

# A New Machine Learning Retrieval of Liquid Water Path Optimized for Mixed-Phase Cold Air Outbreaks Using Radiometer and Radar Observations

SAMUEL EPHRAIM,<sup>a</sup> PAQUITA ZUIDEMA,<sup>a</sup> TIMOTHY W. JULIANO,<sup>b</sup> COLTIN GRASMICK,<sup>c</sup> MARIA CADEDDU,<sup>d</sup> BART GEERTS,<sup>c</sup> JEFF FRENCH,<sup>c</sup> ANDREW PAZMANY,<sup>e</sup> SARAH WOODS,<sup>b</sup>

<sup>a</sup> *Rosenstiel School Department of Atmospheric Sciences, University of Miami, Miami, FL*

<sup>b</sup> *U.S. NSF National Center for Atmospheric Research, Boulder, CO*

<sup>c</sup> *Department of Atmospheric Science, University of Wyoming, Laramie, WY*

<sup>d</sup> *Argonne National Laboratory, Batavia, IL*

<sup>e</sup> *ProSensing, Inc., Amherst, MA*

**ABSTRACT:** Cold-air outbreaks over high latitude oceans typically include mixed-phase clouds and precipitation, in particular supercooled liquid clouds that support snow and graupel through ice growth processes. The partitioning of the total water into the liquid and ice phases impacts both weather and climate prediction, but accurate measurements on the phase partitioning remain difficult to acquire, especially near-real-time. Here we present a machine learning approach to retrieve liquid water path (LWP) using passive microwave measurements combined with vertically-integrated radar reflectivities. The approach is an extension of Cadeddu et al. (2009), with the novel addition of radar reflectivity. The machine learning models are trained using the Passive and Active Microwave radiative TRAnsfer (PAMTRA) code applied to output from numerical simulations of three independent cold-air outbreaks sampled during the Cold-Air Outbreaks in the Marine Boundary Layer Experiment (COMBLE) campaign. Brightness temperatures corresponding to the four sidebands of an upward-looking G-band (183 GHz) Vapor Radiometer, along with the vertically-integrated reflectivity from a zenith-pointing 95 GHz Wyoming Cloud Radar, are simulated from the perspective of a near-surface aircraft track. The radar reflectivity helps discriminate the snow contribution to the brightness temperatures. The machine learning models are thereafter tested on a simulation of an independent cold-air outbreak during COMBLE, and against measurements from the US Department of Energy Atmospheric Radiation Measurement North Slope of Alaska observatory. This machine learning approach is shown to provide robust, computationally-efficient, near-real-time measurements of LWP and water vapor path during the Cold Air Outbreak Experiment in the Sub-Arctic Region (CAESAR) campaign in February-April 2024.

**SIGNIFICANCE STATEMENT:** Precipitation from mixed-phase clouds over the high-latitude open waters impacts shipping, fishing and coastal communities. Mixed-phase clouds are also a modeling challenge, inhibiting weather and climate prediction skill. More comprehensive measurements of the cloud liquid and ice water path occupying the same vertical column improve our understanding and ability to represent this challenging cloud type. Here we propose a new retrieval to determine the liquid water path within air columns that also contain ice.

## 1. Introduction

Cold-air outbreak (CAO) clouds in the Arctic are commonly mixed-phase (MP); however, the partitioning between the amount of ice and liquid in below-freezing CAO clouds and precipitation is not theoretically constrained and also not well observed. The process understanding of how the cloud phases partition as a function of cloud lifecycle is important for the prediction of snowfall rates, convective lifecycle, and intensity at weather timescales. The partitioning into liquid versus ice also has radiative impacts that are consequential for climate (Bodas-Salcedo et al. 2016a), with quiescent, liquid-containing, higher-albedo

MP clouds able to possess a long lifetime despite being microphysically unstable (Zuidema et al. 2005b; Morrison et al. 2012), and warming the surface more effectively than ice clouds through longwave radiation (Korolev et al. 2017). Secondary ice production processes in global models can deplete liquid in high-latitude clouds too readily (Bodas-Salcedo et al. 2016b) while simultaneously predicting too few ice-nucleating particles (McCluskey et al. 2023).

A better understanding of the relevant microphysical processes in Arctic MP CAOs requires accurate and representative measurements of the liquid water path (LWP), as part of a larger suite of measurements of microphysics, kinematics, and thermodynamics. Such measurements are not readily available. Spaced-based microwave satellite retrievals are stymied by large footprints that average over cloud inhomogeneities (Bremen et al. 2002; Elsaesser et al. 2017) and can include surface contributions from sea ice (Zuidema and Joyce 2008), while retrievals based on visible imagery are uncertain because of solar zenith biases and three-dimensional radiative transfer effects (Khanal et al. 2020). Surface-based remote sensing assessments provide finer horizontal detail (Mages et al. 2023; Lackner et al. 2024) but may not capture the cloud evolution as comprehensively as an aircraft characterization (Abel et al. 2017; Seethala et al. 2024). *In-situ* measurements of total

---

Corresponding author: Samuel Ephraim,  
samuel.ephraim@earth.miami.edu

and liquid water content are useful but typically confined to spatial scales of  $\sim 100$  m (Korolev et al. 1998).

Within this suite of measurement strategies, airborne passive microwave measurements provide another path forward (McGrath and Hewison 2001). A recent spate of surface-based field campaigns have focused on high-latitude CAOs, both over the Southern Ocean (Alexandar et al. 2021; Hu et al. 2023), and the northern high latitudes, including the US Department of Energy (DOE) Cold-Air Outbreaks in the Marine Boundary Layer Experiment (COMBLE) Mobile Facility deployment in Andenes, Norway from December 2019 through May 2020 (Geerts et al. 2022; Mages et al. 2023). CAO-focused analyses based on aircraft campaigns include Kirbus et al. (2023), Raif et al. (2024), Wendisch et al. (2024) and Huang et al. (2025). Within these campaigns, only the surface-based campaigns typically include microwave-derived liquid water paths within their process analysis, with Abel et al. (2017) being the exception that also uses aircraft-based microwave liquid water path retrievals within their CAO analysis.

The US National Science Foundation further supported the Cold Air outbreak Experiment in the Sub-Arctic Region (CAESAR) aircraft campaign, based out of Kiruna, Sweden in spring of 2024, aboard the NSF NCAR C-130. A particular strength of the CAESAR campaign is a strong synergistic instrument suite of both *in-situ* and remote sensors. Within the CAESAR instrumentation suite, we focus on the upward-pointing G-band Vapor Radiometer (GVR), a passive microwave radiometer using frequencies near the 183.31 GHz water vapor absorption band, and the 95 GHz Wyoming Cloud Radar (WCR). This instrument has not been used previously within high-latitude airborne mixed-phase cloud analysis to our knowledge.

The GVR measurements are optimal for dry atmospheres, where the sensitivity to small changes in vapor and liquid is high. Surface-based passive microwave measurements near 183 GHz have been applied to Arctic MP clouds over Alaska (Cadeddu et al. 2009), and to subtropical marine clouds using the NCAR C-130 (Zuidema et al. 2012). When applied to convective Arctic MP clouds, the potential presence of snow, at sizes capable of scattering microwave radiation emitted from the surface back downwards towards the GVR, is an additional challenge. This motivates the use of vertically-integrated 95 GHz (W-band) radar reflectivities for identifying the larger ice particles in this study.

To design the machine learning retrieval, the Passive and Active Microwave radiative TRAnsfer (PAMTRA) model (Mech et al. 2020) is applied to model representations of CAO clouds sampled during the COMBLE campaign period (Juliano et al. 2024). Limited-area-model (LAM) simulations use a 1 km horizontal grid cell spacing ( $dx$ ), while a large-eddy-scale (LES) simulation is performed at  $dx = 150$  m. These simulations constitute the training and test

datasets, respectively. Both sets of simulations use similar microphysical schemes. Additional testing uses GVR and 35 GHz Ka-band ARM Zenith Radar (KAZR) data during CAO conditions at the DOE Atmospheric Radiation Measurement (ARM) North Slope Alaska (NSA) site as input into the new retrieval, with the results compared to other available operational retrievals. During CAESAR we validated the retrieved LWPs and WVPs with data from the *in-situ* microphysical probes.

## 2. Data and Methods

One popular physical retrieval approach uses optimal estimation, in which *a priori* data provide the first guess, and a forward model performs a gradient descent until converging on a complete atmospheric state (Zuidema et al. 2005a; Cadeddu et al. 2007; Maahn et al. 2020). The approach provides a quantified error characterization based on the Bayes theorem (Maahn et al. 2020). Optimal estimation approaches are computationally expensive, prohibiting calculation of near-real-time LWP and water vapor path (WVP) estimates. An optimal estimation approach also depends on an *a priori* dataset of representative soundings, potentially drawn from model data. ERA5 reanalysis data have been used to develop WVP and LWP retrievals for other Arctic campaigns (e.g., Walbröl et al. 2022), but ERA5's  $dx = \sim 31$  km is not fully adequate for resolving CAO convective cells. Radiosondes are routinely launched from Jan Mayen and Bjornoya islands in the Norwegian/Greenland Sea, but the data sampling of CAO conditions remains limited.

Statistical retrievals rely on a previously-developed empirical relationship between the measurement and desired atmospheric variable, such as site-dependent monthly retrieval coefficients based on radiosonde datasets, or, further enhanced with additional ancillary measurements (Liljegren et al. 2001). Statistical retrievals can use both linear and nonlinear regressions, or empirical orthogonal functions. While computationally efficient, most statistical retrievals struggle to accurately represent complex relationships between variables (Maahn et al. 2020). In addition, most statistical retrievals do not rigorously account for error propagation, though it can be done stochastically.

Machine learning is a type of statistical retrieval that allows complex nonlinear relationships between variables to be understood. In one example, Cadeddu et al. (2009) trained a neural network using GVR measurements and radiosonde data at the DOE ARM NSA site. This algorithm worked comparably well (or better) than other retrieval techniques in use at the same site. A drawback preventing its application to the CAESAR dataset is that none of the microwave retrievals in place at NSA account for the scattering by snow. In addition, the retrievals can only be applied to the same conditions the surface-based retrievals were developed for.

In this study, we build upon Cadeddu et al. (2009) by adding vertically-integrated 95 GHz radar reflectivities provided by the Wyoming Cloud Radar (WCR; version 4) to articulate the influence of large particle scattering upon the LWP retrieval. The scattering is primarily due to snow for Arctic CAOs. The radar reflectivity is extremely sensitive to snowfall through its dependence on the sixth power of the particle size, and this can inform on the snow’s contribution to the GVR brightness temperatures ( $T_b$ ), as opposed to cloud liquid and water vapor alone. In addition, we provide robust error estimation for each individual retrieval value, by assessing the propagation of select error sources into the retrieval. While this retrieval is developed for pragmatic near-real-time application during the CAESAR campaign, the methods can be adapted to other applications as long as a representative model training data is available.

#### a. Instruments

The GVR measures sky radiances in four sidebands surrounding the 183.31 GHz water vapor absorption band:  $\pm 1$ ,  $\pm 3$ ,  $\pm 7$ , and  $\pm 14$  GHz. The instrument is calibrated using a warm target whose temperature fluctuates near 15 °C and a hot load kept near 60 °C. The measurement error will increase with distance from the calibration temperatures and their difference, impacting the cold  $\pm 14$  GHz  $T_b$  measurement the most. The  $\pm 1$  GHz sideband is 30 times more sensitive to WVP than the  $T_b$  measured at 23.8 GHz by the more commonly used two-channel microwave radiometer (MWR) at WVP  $< 2.5 \text{ kg m}^{-2}$  (Cadeddu et al. 2009). The  $\pm 7$  GHz and  $\pm 14$  GHz wing channels are 2-3.5 times more sensitive to LWP than the 31.4 GHz channel of a conventional MWR (Cadeddu et al. 2009; Zuidema et al. 2012). In more moist conditions, the channels nearest to the absorption band begin to saturate; however, the furthest wing channels retain sensitivity to moisture and cloud water for WVPs below  $20 \text{ kg m}^{-2}$ . We therefore expect the thermodynamic conditions characterizing the wintertime CAOs over the Norwegian/Greenland Sea to support useful LWP retrievals. The high  $T_b$  sensitivities to small amounts of integrated liquid and vapor make the GVR an ideal instrument for observing LWP and WVP in a cold, relatively dry environment supporting super-cooled liquid.

The airborne GVR, documented in Pazmany (2007), was first developed for use on the University of Wyoming King Air research aircraft (Wang et al. 2012), modified from a surface-based design built for northern Alaska (Cadeddu et al. 2009). The airborne GVR was subsequently leased from the manufacturer ProSensing for fieldwork in the southeast Pacific held in 2008 (Zuidema et al. 2012). The next deployment of the GVR was for the CAESAR campaign. The GVR was examined prior to the deployment at the manufacturer, and outfitted with a new data computer.

Liquid nitrogen calibration is not used, with confidence placed in using the warm/hot loads to provide consistent real-time calibration. The GVR was brought to the ARM SGP site in October-November 2023, where its measured  $T_b$  could be compared with that calculated from nearby radiosondes. This is discussed in Section 3. During the CAESAR deployment,  $T_b$  oscillations, with amplitudes that occasionally exceeded 10 K, occurred with a period of  $\sim 30$ -60 seconds. These were associated with the internal warm load heater turning on. For most below-cloud legs during CAESAR, the heater was turned off to eliminate the oscillations. However, many of the above cloud WVP retrievals have oscillations of  $\sim 250$ -500  $\text{g m}^{-2}$  because of the heater-induced  $T_b$  oscillations. An example is shown in Section 7. These oscillations propagate into the LWP and WVP retrievals. Time periods where oscillations are present are flagged in the published dataset.

The WCR-4 (University of Wyoming - Flight Center 1995) has three directional antennas when installed on the C-130. We use the upward-pointing single-polarization beam for the retrieval. The WCR calibration constant is determined using the return from a trihedral corner reflector with a known backscatter cross-section. Calibration was performed once before CAESAR and twice after CAESAR with the calibration constant varying by less than 2 dB. An additional uncertainty of 0.5 dB was present from antenna cross-calibration, resulting in a total uncertainty in the absolute calibration of reflectivity of approximately 2.5 dB.

The LWP retrieval was compared to vertically-integrated *in-situ* liquid water contents (LWCs) derived from two *in-situ* probes: a King probe and the inboard Cloud Droplet Probe (CDP) measuring cloud droplet size distributions spanning 3 to 50  $\mu\text{m}$  in diameter (Lance 2012), gathered during spiral profiles within a vertical column. The WVP retrieval was validated using the Buck hygrometer. These comparisons are explained further in Section 6.

#### b. LES and LAM Simulations of CAOs

The retrieval is trained on numerical simulations using the Weather Research and Forecasting (WRF) model (Skamarock and Klemp 2008; Skamarock et al. 2019). We use LAM simulations of three different CAOs sampled during the COMBLE campaign: 28 March 2020, 10 April 2020, and 26 April 2020 (Juliano et al. 2024). The LAM is configured using a nested, two domain setup (one-way feedback), with the outer and inner domains resolved to  $dx = 3 \text{ km}$  and  $dx = 1 \text{ km}$ , respectively. For this study, we use outputs from only the inner domain corresponding to the light blue box in Figure 1. The Mellor-Yamada-Nakanishi-Niino eddy-diffusivity/mass-flux planetary boundary layer (PBL) parameterization (Olson et al. 2019) is activated for the 28 March case, while the Yonsei University (YSU) PBL parameterization (Hong et al. 2006)

is activated for the other two cases. The use of different PBL schemes yields a broader training dataset. In addition, the LAM simulation uses the Thompson-Eidhammer aerosol-aware microphysics parameterization (Thompson and Eidhammer 2014). This scheme can represent cloud condensation nuclei and ice nucleating particles prognostically (including precipitation scavenging). Recent advancements to the WRF model, as detailed by Juliano et al. (2022), enable the incorporation of time-varying aerosol fields from the GEOS-5 model. Additional details about the LAM configuration, including the physics parameterizations, may be found in Juliano et al. (2024).

To test the retrieval, we use model outputs from a separate WRF simulation of a 13 March 2020 CAO (Fig. 1). This simulation consisted of a mesoscale domain ( $dx = 1050$  m) containing (2161,2201) grid cells in the (x,y) direction, spanning (2269,2311) km. This was coupled online (one-way feedback) to a very large LES domain (dark blue box in Fig. 1), resolving the Fram Strait at  $dx = 150$  m. The LES domain contained (3780,8400) grid cells at  $dx = 150$  m, thus spanning (567,1260) km. The vertical grid was the same on both domains and contained 136 grid cells. First, the mesoscale domain was integrated from 12 to 22 UTC on 12 March, at which point the LES domain was activated, and the two domains integrated simultaneously while coupled online until 00 UTC on 14 March. The mesoscale domain uses the YSU PBL scheme and the LES domain uses the three-dimensional, turbulence kinetic energy-based subgrid-scale scheme of Deardorff (1980). For both domains, the vertical grid structure and other physics options, including the microphysics scheme, are identical to those settings for the LAM simulations.

Our four selected cases span a subjectively-determined range of CAO conditions sampled during COMBLE, described further in Lackner et al. (2024). The 26 April case, consisting of closed cellular convection, was one of the weaker cases, while 10 April was a moderately strong CAO case containing open cellular convection. Meanwhile, the 13 March (Fig. 1) and 28 March events were the two strongest observed during the COMBLE campaign, with large open cells and cloud top heights on 13 March reaching 3-5 km. These events were realistically depicted by the LAM simulations (Juliano et al. 2024). Underscoring the need to account for the snow’s impact on the  $T_b$ , the snow water path (SWP) within a region of open celled convection (small red box in Fig. 1, spanning 15 km by 15 km) is shown to dominate the total water path in Figure A1b.

### c. PAMTRA

We use PAMTRA to calculate  $T_b$  and vertically-integrated radar reflectivities from the LES and LAM simulation outputs. PAMTRA is a forward radiative transfer

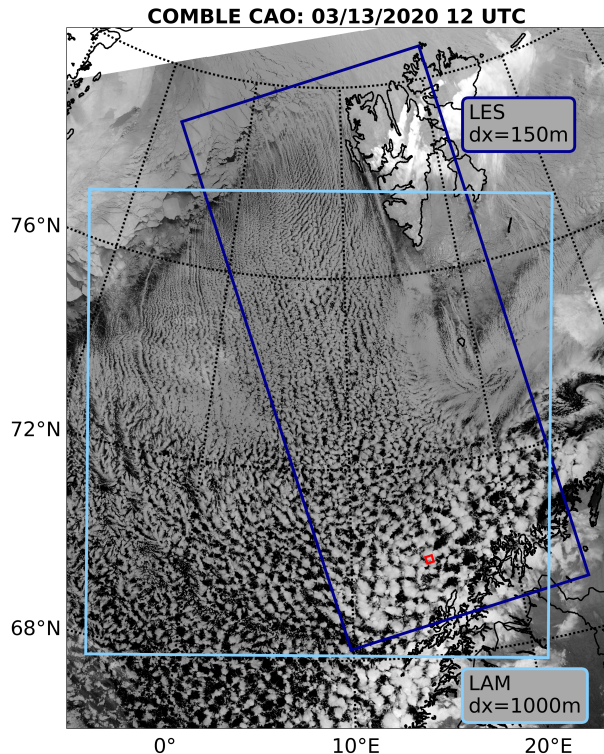


FIG. 1. NOAA-20 VIIRS infrared satellite image of the CAO cloud field at ~12 UTC on 13 March 2020. LES and LAM domains are shown in the dark blue and light blue boxes, respectively. The red box at 70° N, 15° E is detailed further in Fig. 2 and in Appendix A.

model capable of simulating both active and passive microwave measurements (Mech et al. 2020) and has also been applied to data from other Arctic campaigns (e.g., Walbröl et al. 2024).

Figure 2 shows the  $T_b$  at  $183.31 \pm 14$  GHz and the vertically-integrated 95 GHz reflectivities calculated by PAMTRA for the open-celled convection test section shown in Figure 1, after including all hydrometeors and water vapor, while Figure A1 indicates the contributions to  $T_b$  and reflectivity from the individual hydrometeors. Figures 2 and A1 are only one snapshot of the LES simulation, but represent characteristics of the full simulation based on inspection of many such snapshots. Of the six hydrometeors considered (LWP, SWP, ice water path (IWP), graupel water path (GWP) and WVP), the LWP has the strongest influence on  $T_b$  (Fig. A1ai). Nevertheless, the  $T_b$  contribution from snow is also substantial (Fig. A1bi) and that from graupel (Fig. A1di) cannot be neglected. The contributions to radar reflectivity are dominated by snow (Fig. A1bii) and graupel (Fig. A1dii). Rain is infrequently present in the modeled CAOs over the Norwegian/Greenland Sea and is not shown, while ice crystals contribute negligibly to both the  $T_b$  and radar reflectivities (Figs. A1ci,cii).

From Figure A1, we can infer that the microphysical representation of the snow is important to both the  $T_b$  and radar reflectivity. The user interface of PAMTRA allows for a variety of microphysical schemes, and supports a fine-tuning towards the anticipated microphysics. Adjustable parameters include the axial ratio (AR; the ratio of the major and minor axes of a hydrometeor), the area-size and mass-size relationships for frozen, non-spherical hydrometeors, and gamma distribution descriptions of all the particle size distributions, using a shape parameter  $\mu$  to establish the distribution widths. The relationship between a hydrometeor’s diameter,  $D$ , and mass,  $M$ , is defined as  $M = aD^b$ . The value of  $b$  will vary between 2 (for a thin circular plate) to 3 (for a perfectly spherical hydrometeor). Similarly, the projected surface area,  $A$ , relates to  $D$  as  $A = \alpha D^\beta$ . PAMTRA uses the self-similar Rayleigh-Gans approximation (Hogan et al. 2017) for simulating frozen hydrometeors. For snow and graupel, the largest uncertainty in simulated  $T_b$  and reflectivity is from the choice of the mass-size parameters,  $a$  and  $b$ . The mass-size and area-size relationships are both highly dependent on the amount of rime, which varies significantly spatially and temporally. As a particle’s rime fraction increases, it becomes more spherical and more dense. Using this knowledge, Mason et al. (2018) developed a line of best fit from past research campaigns of  $a$  versus  $b$  and  $\alpha$  versus  $\beta$  along a continuum of density factors ( $\rho$ ) stretching from  $\rho = 0$  for unrimed aggregates measured in cirrus clouds (Brown and Francis 1995), to  $\rho = 1$  for spheres of solid ice. A snow density factor of  $\rho = 0.2$  and a graupel density factor of  $\rho = 0.7$  are used to calculate  $a$ ,  $b$ ,  $\alpha$ , and  $\beta$  following Mason et al. (2018).

In addition, the AR value depends on the dominant snow morphology. We specify an AR = 0.6 for snow following Mason et al. (2019), with the reflectivity insensitive to AR variations near that value (Mason et al. 2019). The final important microphysical choice for snow and graupel is the shape parameter,  $\mu$ . Values of  $\mu > 0$  generate a distribution that is broader than an exponential distribution, while a distribution with  $\mu < 0$  is narrower than an exponential distribution. Higher  $\mu$  values increase the number concentration of large hydrometeors relative to small ones, which especially affects radar reflectivity. Mason et al. (2018), using a triple radar retrieval of snow-containing clouds in Finland, document  $\mu = -1$  for snow (in agreement with Brandes et al. 2007), and  $\mu = 5$  for graupel. Graupel is represented using a single moment in the LES/LAM simulations. We set the effective radius to 0.7 mm. This value falls on a plateau region in the dBZ versus effective radius relation (Sieron et al. 2017), and a small change in the effective radius choice doesn’t noticeably impact the calculated reflectivity. The microphysical parameters chosen for the frozen hydrometeor species most impactful for the LWP retrieval are summarized in Table 1.

	AR	$a$	$b$	$\alpha$	$\beta$	$\mu$
Snow	0.6	0.0908	2.12	0.0878	1.774	-1
Graupel	1	14.01	2.67	n/a	n/a	5

TABLE 1. Microphysical parameters used for the frozen hydrometeors simulated in PAMTRA: The axial ratio (AR), mass-size relation variables ( $a$  and  $b$ ), area-size relation variables ( $\alpha$  and  $\beta$ ), and the shape parameter ( $\mu$ ).

The  $T_b$  from the liquid water is not impacted by the size distribution of cloud droplets as long as the radiative transfer falls within the Rayleigh regime. At the GVR wavelength of 183.31 GHz, contributions from Mie scattering are negligible as long as the drop sizes remain smaller than 1.5 mm. The radar reflectivity is nevertheless affected weakly by the shape parameter,  $\mu$ . We use a  $\mu = 9.6$  for cloud droplets based on Miles et al. (2000). Contributions from the Mie absorption/emission can begin at drop diameters of 50  $\mu\text{m}$ , however (See Appendix A of Zuidema et al. (2005a)), increasing with colder temperatures. The impact on the  $T_b$  depends on the relative contribution of drizzle/rain to the total water path. In the LES/LAM simulations, drizzle/rain was barely present, and we neglect its potential contribution to the observed  $T_b$ s in this study, but can revisit it with CAESAR data in future work.

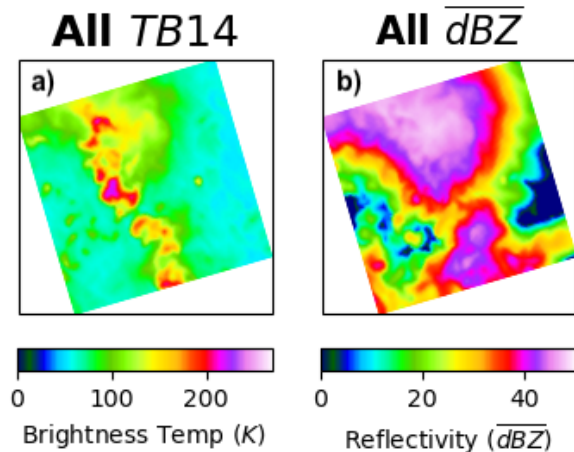


FIG. 2. PAMTRA-simulated (a) 183.31  $\pm$ 14 GHz  $T_b$  and (b) vertically-integrated 95 GHz reflectivities ( $\overline{dBZ}$ ) from all hydrometeors within the 15x15 km ( $dx = 150$  m) open-celled test section (red box in Fig. 1).

#### d. Data Preprocessing

The sampling of every gridpoint from the LES and/or LAM models is not practical due to the runtime constraint on PAMTRA. Cloud liquid and snow are the primary heterogeneously-distributed variables influencing  $T_b$  and reflectivity. Therefore, we apply a weighted random selection method to the training/test points over the ocean, such

that their two-dimensional histogram (LWP x SWP) span the full range of anticipated conditions. The probability of a given LAM/LES gridpoint being selected was experimentally determined and set to an inverse exponential dependent on the number of points in a given LWP/SWP bin. An example of the selection method is shown in Fig. 3. This also increases the range of WVPs sampled while reducing the sampling of clear-sky points. Testing/training points vary both horizontally across the model domain and vertically up to 5000 m to simulate the variety of airborne sampling locations. This sampling method is applied to both the LAM and LES model output, generating approximately 600,000 training points and 100,000 testing points.

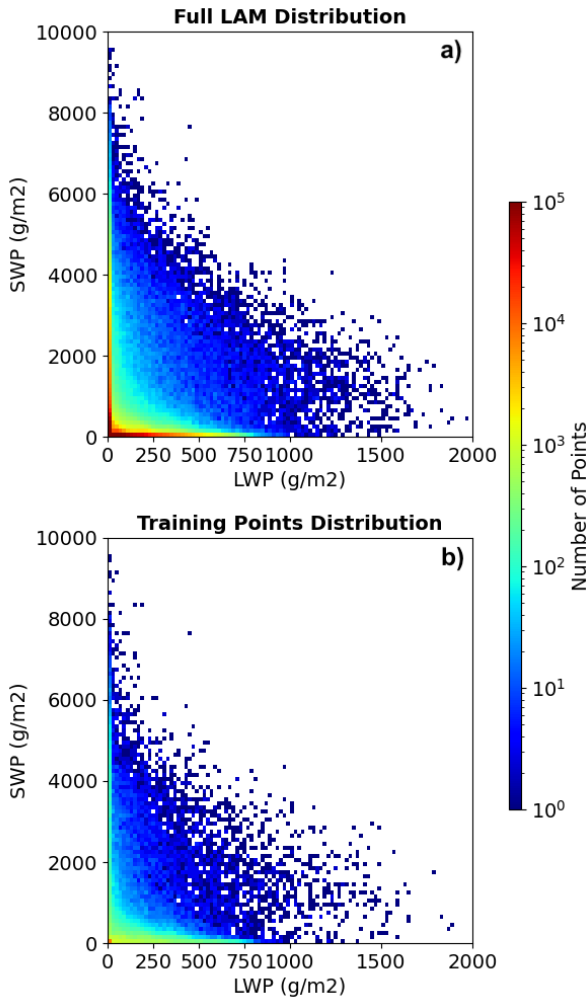


Fig. 3. Distribution of LWP/SWP in a) all LAM model runs and b) selected training points. The selection probability for training points followed  $P = e^{-N*0.001}/3 + 0.005$  where N is the number of LAM points across all three model runs in a given LWP/SWP bin. A similar method (not shown) is applied on the LES run to determine the test set.

The four radiometer measurements are sensitive to the full atmospheric column with the presence of snow introducing uncertainty within the LWP and WVP retrievals. In keeping with this low-dimensionality, the radar reflectivities are vertically-integrated, producing a single value at each spatial gridpoint, using  $\overline{dBZ} = 10 * \log_{10} \int_{z_i=FL}^{z_i=TOA} Z_{e,i} dz$ , where  $Z_{e,i} = 10^{\frac{1}{10} dBZ_i}$ . Any final integrated reflectivity less than -20 dBZ was set to -20 dBZ. When reflectivities are below -20 dBZ, either no snow is present, or is present in small enough quantities that the impact on GVR  $T_b$  is negligible. The -20 dBZ threshold maximizes model performance. The pitch/roll angle is taken into account by correcting for the increased path length, though errors at large aircraft zenith angles are likely larger.

#### e. Machine Learning Approaches

Two machine learning approaches, with different sensitivities to input errors, are investigated. One is a neural network regression and the other is a random forest regression. For both methods, the input is a vector of length 5 containing the 183.31 GHz  $\pm 14$ ,  $\pm 7$ ,  $\pm 3$ , and  $\pm 1$  GHz  $T_b$  and the vertically-integrated 95 GHz radar reflectivity. Noise is not added to the training data. The output is LWP or WVP. While this may suggest an overconstrained solution, we cannot control well for other influencing variables, such as the vertical structure of temperature and humidity. This is the reason for selecting model simulations of the same cloud regime for the training and testing datasets.

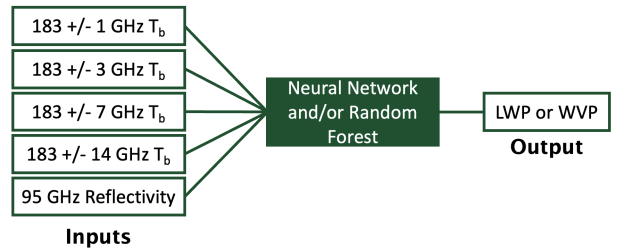


Fig. 4. Inputs and outputs of the machine learning retrieval. Neural network and random forest models are run separately and then averaged together for the LWP retrieval. Random forest is solely used for the WVP retrieval. Note the reflectivity is a vertically-averaged quantity.

The neural network approach uses a Multilayer Perceptron Neural Network (MLPNN) based on the MLPRegressor model within the sklearn Python package (Pedregosa et al. 2011). MLPNNs are used for complex regression tasks across many disciplines and can identify complex non-linear relationships between variables. Hyperparameters were tuned using 5-fold validation testing on the training dataset using the sklearn RandomizedSearchCV algorithm. RandomizedSearchCV tests the performance of the model on randomly selected hyperparameters across a predefined phase space and chooses the combination with

the highest skill. The skill metric we decided to use was the root-mean-square-error (RMSE). We tested 500 different combinations of hyperparameters. The architectures tested include a single layer with up to 500 nodes, two layers with up to 250 nodes per layer, and three layers with up to 100 nodes per layer. Other hyperparameters varied were the activation function (Rectified Linear Unit (ReLU), tanh, logistic) and alpha (0.01, 0.001, 0.001). We used the Adam optimizer (Kingma and Ba 2017), as that was the only solver that converged in 500 iterations. The ReLU activation function was optimal for all of our MLPNNs. Choice of architecture and alpha for our MLPNNs is shown in Table 2. Defaults are used for all other hyperparameters.

The other machine learning approach is a Random Forest (RF) Regressor, also from the sklearn Python package. The RF Regressor uses an ensemble of decision trees generated through bootstrapping the training dataset. The output of each of the decision trees is then averaged to generate a prediction. The RandomizedSearchCV algorithm was also used to tune the RF hyperparameters by varying the number of estimators from 1-50 and the criterion (squared error, absolute error, friedman mse, poisson). The optimal criterion was squared error, and the performance increased asymptotically as the number of estimators was increased. Thus, all of our RF Regressors use 50 estimators and the squared error criterion. All other hyperparameters are left as defaults.

For the LWP retrievals, both the MLPNN and RF performed as well individually as when their outputs were averaged, both during model testing (Section 4) and testing using NSA datasets (Section 5), with differences in r-squared  $< 0.01$ . We nevertheless chose to average both outputs to reduce variability. For the WVP retrievals, the RF performed significantly better than the MLPNN (differences in r-squared of  $\sim 0.05$ ). Thus, the operational WVP retrieval only uses a RF. In summary, LWP and WVP are retrieved separately, producing three machine learning models in total: a neural network for the LWP retrieval, and a separate random forest for the LWP and WVP retrievals.

### 3. ARM Southern Great Plains GVR Calibration Testing

From October 30 to November 10, 2023, the GVR was deployed to the DOE ARM Southern Great Plains (SGP) site to assess the GVR calibration  $T_b$ . The  $T_b$ s measured by the GVR during clear-sky conditions, determined using the Total Sky Imager (Flynn and Morris 2023), are compared to those simulated by PAMTRA based on the SGP radiosondes (Keeler et al. 2023) in Figure 5. Overall, the clear-sky GVR  $T_b$ s are warmer than those simulated by PAMTRA, especially under drier conditions and by the far wing channels, by up to 15 K (Fig. 5a). The PAMTRA simulations rely on the Rosenkranz (1998) water vapor emission model. A sensitivity test relying on the MonoRTM

(Clough et al. 2005) emission model slightly decreases the simulated  $T_b$  (increasing the bias relative to the GVR), by approximately 1-2 K. This small difference between radiative transfer models indicates most of the discrepancy is from a miscalibration of the GVR.

The best-estimate of the bias as a function of the measured  $T_b$  (black solid line in Fig. 5b) is used to post-process the GVR  $T_b$ s during CAESAR. The bias correction also improved a high bias noted in the real-time retrieved LWP and WVP estimates during the campaign.

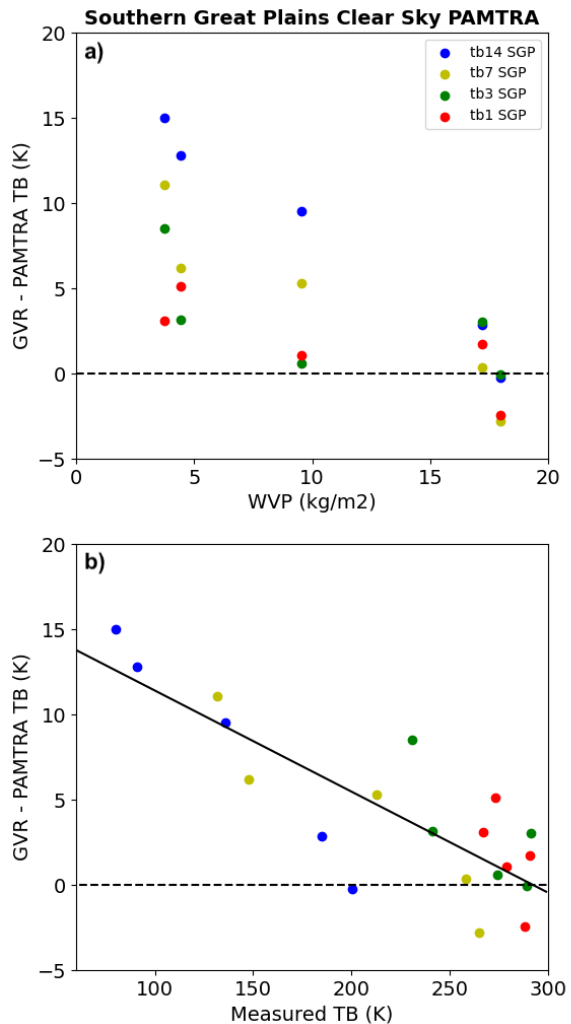


FIG. 5. Bias of GVR  $T_b$ s in clear sky conditions using radiosonde data with respect to PAMTRA-simulated  $T_b$ s at the ARM SGP field site as a function of a) radiosonde-observed WVP and b) GVR  $T_b$ .

### 4. Machine Learning Model Testing

Training is conducted on selected points from LAM simulations of three independent CAOs encompassing

## MLPNN Hyperparameters

Model	Architecture	Alpha
LWP Operational	(20,70,60)	0.0001
LWP No WCR	(50,20,90)	0.01
LWP NSA	(40,60,100)	0.0001

TABLE 2. Hyperparameter choices for all of our MLPNN models: The operational LWP retrieval, the LWP retrieval that does not use the WCR as input (Fig. 6c), and the LWP retrieval used in the ARM North Slope Alaska Site Testing in Section 5.

the full range of possible conditions over the Norwegian/Greenland Sea, referred to as PAMTRA-train. The test dataset, a PAMTRA simulation of an LES run of a CAO from 13 March 2020, is referred to as PAMTRA-test.

### a. Control

The control test determines the LWP and WVP for the PAMTRA-test cases based only on the simulated GVR  $T_b$ s and radar reflectivities. These values are then directly compared to model diagnostics (Fig. 6a-b). The model performed well, with explained variances of 99% and 100% for the LWP and WVP retrievals, respectively. However, this assumes perfect information. When the reflectivity is neglected within retrieval, the retrieved LWPs are clearly biased low, while the retrieved WVPs are only slightly worse (Fig. 6c-d).

### b. Error Estimations

The impact of GVR instrument error, and error in the representation of the microphysical size distributions is considered here. Random instrument error is simulated by perturbing each PAMTRA-test  $T_b$  randomly using a normal distribution with a standard deviation of 2 K, the stated uncertainty of the GVR measurements (Cadettu 2011). The random instrument error in WCR reflectivity is neglected because variability in the reflectivities is dominated by perturbations in the snow/graupel microphysical parameters. Errors within the mass-size and area-size relationships of snow and graupel are evaluated by perturbing the snow/graupel density factors  $\rho$  within separate PAMTRA simulations of the 13 March 2020 LES case, leading to different mass-size and area-size relationships.  $\rho$  is perturbed by  $\pm 0.1$ , corresponding to less riming ( $\rho_{snow} = 0.1$  and  $\rho_{graupel} = 0.6$ ) and more riming ( $\rho_{snow} = 0.3$  and  $\rho_{graupel} = 0.8$ ) than in the control run.

Performance metrics of WVP and LWP retrieved from below, shown in Tables 3-4 and Figures 6e-f, indicate the performance degrades as expected when errors are propagated into the retrieval, but much of the skill is still retained. In the LWP retrieval perturbed test, absolute errors increase as the LWP grows; however, the percent error decreases. Retrievals for LWPs greater than  $100 \text{ g m}^{-2}$  have  $< 20\%$  error. For WVPs, the perturbations produce  $< 8\%$  error.

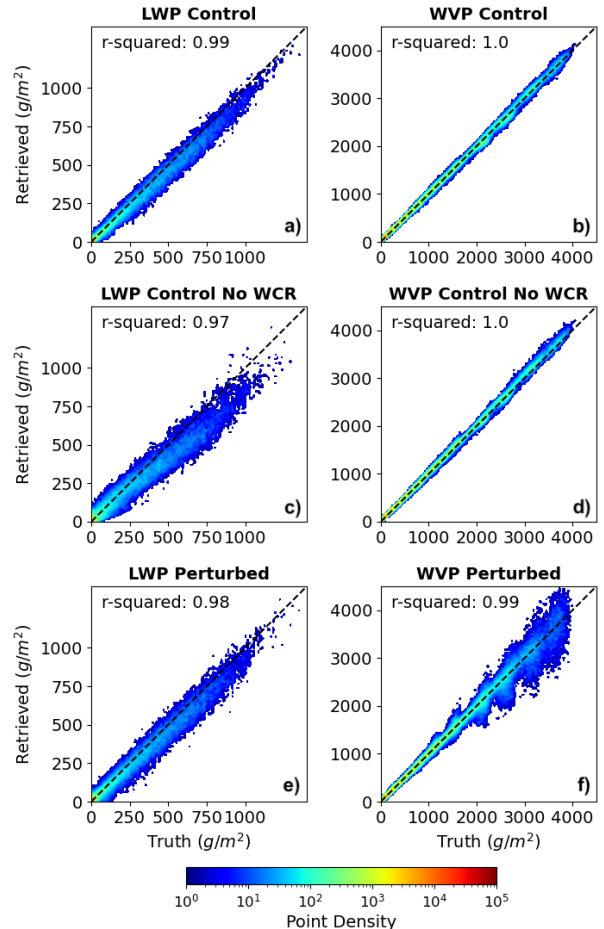


FIG. 6. Performance of both the LWP and WVP retrievals in a) and b): the control test; c) and d): the control test with reflectivity excluded from both the training or testing; e) and f): random perturbations representing instrument  $T_b$  errors and uncertainty in microphysical specifications (for snow and graupel)

The WVP retrieval also has very little bias, as the standard deviation of the residuals roughly equals the RMSE.

## 5. ARM North Slope Alaska (NSA) Site Testing

The retrieval was further tested on data from the ARM NSA site in Utquigvik, Alaska (formerly Barrow). CAO conditions are frequent in Utquigvik during October, when

LWP Performance ( $\text{g m}^{-2}$ )

	25-50	50-100	100-250	250-500	500-1000	> 1000
Control RSME	13.9	19.5	32.3	55.0	77.8	79.9
Control Residual Std	13.7	18.2	27.5	42.7	51.0	48.3
Control % Error	28.9%	20.0%	15.6%	12.1%	9.5%	6.3%
Perturbed RMSE	19.7	26.8	41.3	62.3	87.5	107.1
Perturbed Residual Std	19.6	25.9	37.3	51.7	64.6	80.5
Perturbed % Error	43.4%	28.3%	19.4%	13.6%	10.4%	8.0%

TABLE 3. Performance metrics (root-mean-square error as absolute, a percentage and spread of the residuals) for both control and perturbed LWP datasets binned by the truth LWP.

WVP Performance ( $\text{g m}^{-2}$ )

	250-500	500-1000	1000-2000	2000-3000	3000-4000	>4000
Control RMSE	21.2	27.2	34.0	66.4	66.5	58.0
Control Residual Std	17.5	25.6	33.5	65.8	63.9	39.1
Control % Error	5.2%	2.8%	1.8%	2.2%	1.6%	1.4%
Perturbed RMSE	24.2	35.7	63.8	179.3	300.4	373.7
Perturbed Residual Std	22.3	35.3	63.7	178.7	298.6	372.5
Perturbed % Error	5.6%	3.9%	3.2%	5.2%	6.9%	8.0%

TABLE 4. Performance metrics (root-mean-square error as absolute, a percentage and spread of the residuals) for both control and perturbed WVP datasets binned by the truth WVP.

the Beaufort Sea is still ice-free (Wang et al. 2016). The presence of CAOs at the ARM NSA site is identified using the  $M$  index, defined as  $M = \theta_{SST} - \theta_{850hPa}$  where  $\theta$  is potential temperature (Kolstad and Bracegirdle 2008), SST corresponds to the average SST over a  $2^\circ$  latitude by  $4^\circ$  longitude box due north of the NSA site using the NOAA/NCEI  $1/4^\circ$  Daily Optimum Interpolation Sea Surface Temperature (OISST; Reynolds et al. 2007). The 850 hPa temperature is identified from the NSA radiosondes (Keeler et al. 2023). When  $M$  is positive, the atmosphere is thermally unstable. An additional criterion is that the sea ice concentration, based on the NCEP and GSFC sea ice product, is  $< 33\%$  in the same box. These criteria identified six CAOs spanning a total of 104 hours from 2020 and 2021.

The site includes a surface-based GVR radiometer (Cadeddu and Tuftedal 2021), a 35 GHz Ka-band ARM Zenith Radar (KAZR) (Feng et al. 2021), and independent LWP and WVP retrievals to compare against. For this test, PAMTRA simulates the LAM training case reflectivities at 35 GHz to match the KAZR. All other methods used are the same. The three independent retrieval methods include Turner et al. (2007) and two different retrievals from Liljegren (2004). Turner et al. (2007) is an optimal estimation retrieval utilizing both infrared and microwave (MWR) measurements, and relies on the MonoRTM code. Liljegren (2004) developed two statistical retrievals, one based on measurements from all channels of a 12-channel profiler radiometer (MWRP), and the other on only two channels of

the MWRP. Liljegren (2004) uses the Rosenkranz (1998) water vapor absorption model, similar to our retrieval.

Comparisons to the three other retrievals indicate relatively good agreement (Fig. 7). We note that even though the Turner et al. (2007) and Liljegren (2004) retrievals are well established, this comparison is still different from comparing to truth. Inherent errors may be common to all the retrievals in addition to the instruments. Nonetheless, this comparison provides a high quality sanity check.

## 6. Implementation During CAESAR

The new retrieval supported near-real-time LWP and WVP estimates during CAESAR, with a time latency of less than 10 seconds on-board the plane. An on-board dashboard developed by the first author depicted the most recent 30 minutes of GVR  $T_b$ , WCR integrated reflectivity, the newly-formed LWP and WVP retrievals (including their uncertainty estimates), plane altitude and air temperature. The near-real-time LWP estimates available during the below cloud legs helped inform how much icing might be experienced on the subsequent ascent. The estimates also aided a robust understanding of environmental and cloud conditions helpful for the other instrument teams. The real-time WVP was often useful for determining boundary layer growth, and for identifying sharp moisture boundaries designating different air masses, enabling decisions to resample a given area.

CAESAR also provided an excellent, independent opportunity to validate the GVR-based retrieval. LWCs from the inboard CDP and the King probe are integrated from

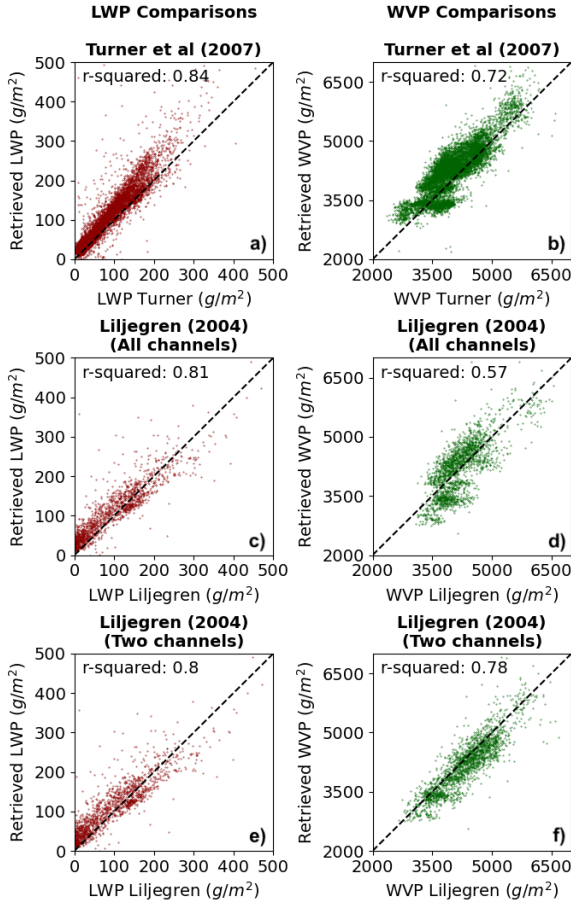


Fig. 7. Comparison of our LWP and WVP retrievals to other retrievals in use at the ARM NSA site.

ascents and descents through clouds, and compared to the three-minute averages of retrieved LWP during the adjacent below-cloud leg. Due to the heterogeneous distribution of cloud water, the comparison relies only on spiral ascents and descents through homogeneous cloud (or clear-sky) layers. Eight spiral ascents/descents (two clear sky and six through cloud) met this criteria across four research flights (RF02, RF04, RF06, and RF07, occurring on 29 February 2024, 3 March 2024, 12 March 2024, and 16 March 2024 respectively).

In contrast, water vapor is more horizontally homogeneous than cloud LWC, and almost all aircraft profiles contributed to the comparison. Both spiral and in-line ascents/descents in all cloud conditions (including clear sky) totaling 97 ascents/descents across all research flights, were analyzed. The WVP constructed from best-estimate specific humidities as measured by a Buck hygrometer during ascents/descents is compared to the retrieved WVP difference between the bottom and top of the ascent/descent.

Prior to a correction to  $T_b$  applied based on the SGP data (Fig. 5), the retrieved LWP was biased high by ( $\sim 75 \text{ g m}^{-2}$ )

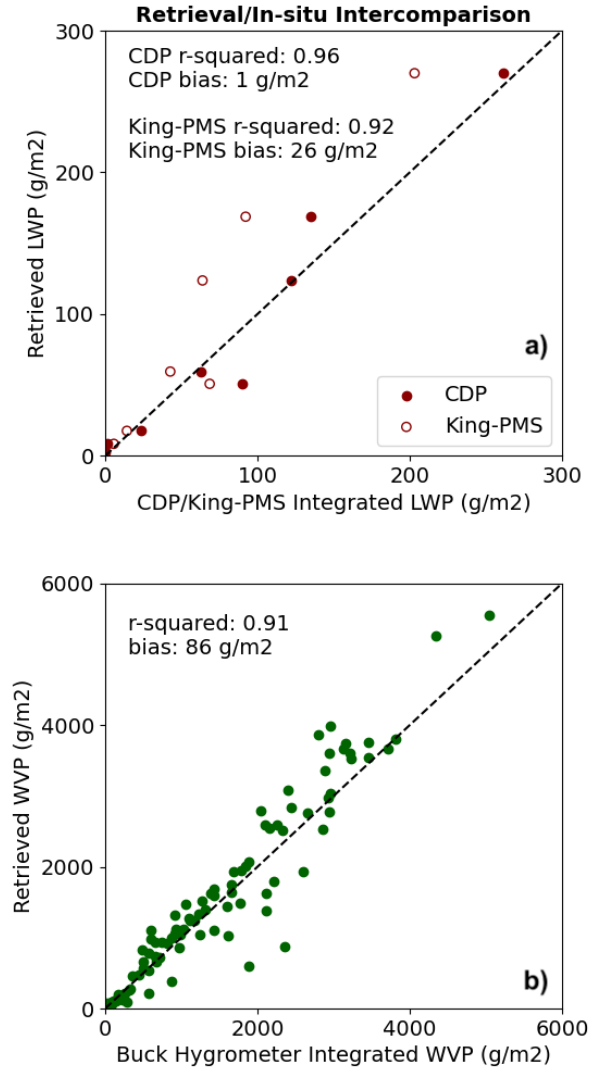


Fig. 8. a) Retrieved LWP versus the integrated *in-situ* LWC from the CDP and King-PMS probes, after both SGP and clear sky LWP bias corrections are applied. b) Retrieved WVP (after SGP bias correction) versus the integrated *in-situ* specific humidity (from both Buck Model 1011C dew-point hygrometers) for defined air layers.

and WVP by ( $\sim 200 \text{ g m}^{-2}$ ) when comparing to the *in-situ* probe data. This is consistent with a sensitivity of  $\pm 14 \text{ GHz } T_b$  to LWP of  $\sim 0.206 \text{ K/g m}^{-2}$  (Ulaby et al. 1986), or a bias in the  $\pm 14 \text{ GHz } T_b$  of around  $15 \text{ K}$  - of a similar magnitude observed at ARM SGP. After adjusting the  $T_b$ s using data presented in Figure 5 from the ARM SGP site, the magnitude of this positive bias in the LWP retrieval reduced to  $\sim 28 \text{ g m}^{-2}$  and the WVP bias nearly disappeared. The magnitude of this LWP bias was determined by averaging the retrieved LWP over  $\sim 75$  minutes of clear-sky portions of surface legs across all research flights. Based on this assessment, a constant offset of  $28 \text{ g m}^{-2}$  was fur-

ther removed from each retrieved LWP. This approach is common within the surface-based microwave radiometry community, e.g., Gaussiat et al. (2007).

The retrieved LWP explains 92%-96% of the variance within the *in-situ* measurements after both bias corrections (SGP and clear sky) are incorporated (Fig. 8a). The final bias is 1 and 26  $\text{g m}^{-2}$  relative to the CDP and King probes, respectively. The King probe is known to underestimate the contribution of the larger drop sizes (Lance 2012), while the CDP probe is calibrated with glass beads and has a sizing uncertainty of 10-20% (Lance et al. 2010). The performance of the CDP was deemed superior to that of the King probe during CAESAR. As such the LWP estimates can be considered to be within the bounds of the uncertainties of the two cloud probes.

## 7. Selected Results

An example is shown from a closed-to-open cell transition sampled on 29 February (RF02) from 15:15 UTC to 15:55 UTC (Figure 9). During the closed cell regime, LWPs are relatively constant around 200-300  $\text{g m}^{-2}$ . The transition to open cells is evident by 15:40 UTC, after which LWPs are much more variable. Maximum LWPs exceeding 500  $\text{g m}^{-2}$  align with *in-situ* updrafts (Fig. 9b). Slight ice precipitation during the closed cells becomes more pronounced after the transition, offset from the LWP local maxima. Although the relative LWP uncertainties within the open-celled region appear to decrease, we note that without more analysis of the snow characteristics our confidence in the uncertainty estimate also becomes less, especially if super-cooled drizzle or rain is also present. Nevertheless, the magnitude and pattern of retrieved LWPs across the transition closely resembles that documented by (Abel et al. 2017) during a CAO north of the UK at warmer temperatures. The WVPs above the aircraft increase slightly from  $\sim 3000$  to  $\sim 3500$   $\text{g m}^{-2}$  as the boundary layer grows. In contrast, the free tropospheric WVP above  $\sim 2$  km decreases from  $\sim 2000$   $\text{g m}^{-2}$  at 15:15 UTC to  $< 500$   $\text{g m}^{-2}$  at 15:57 UTC, indicating a free-tropospheric air mass boundary. Heater-induced oscillations are evident before 15:22 UTC, most evident in TB1 (Fig. 9f).

The retrieved LWPs in combination with *in-situ* vertical velocities and IWC derived from the Nevzorov probe (Korolev et al. 1998) also provides indications of the age of the convective cells, of which 3 are labeled in Fig. 9a-d. Cell 1 has a strong LWP core with a well-defined updraft and is precipitating ice in regions outside the main updraft. This suggests cell 1 is in a mature stage. In contrast, cell 2 has no apparent liquid water, with intense ice precipitation. The full glaciation, supported by the high radar reflectivities and active precipitation suggests the cell is likely decaying. Cell 3 has a LWP core and a distinct updraft region, but no IWC, indicating a young cell that has not yet started precipitating.

A survey of all the retrieved CAO LWPs and WVPs (Fig. 10) indicates most CAO clouds possess LWPs  $< 200$   $\text{g m}^{-2}$ , with some LWP values approaching or exceeding 1000  $\text{g m}^{-2}$ . We hypothesize these are from strong convective updrafts in open celled convection. Such updrafts may contain drops of sufficient size that Mie absorption/emission increases the  $T_b$ , unphysically increasing the retrieved LWPs (Cadeddu et al. 2017). These conditions require further scrutiny. WVPs above the aircraft retrieved during the  $\sim 300$  m near-surface level legs vary from flight to flight based on the background synoptic conditions, ranging from 1000  $\text{g m}^{-2}$  to 7000  $\text{g m}^{-2}$ .

## 8. Conclusion

A new technique capable of discriminating the liquid phase within mixed-phase clouds using microwave radiometer has become available. An important and novel addition is that of the vertically-integrated radar reflectivity, towards better constraining the contribution of snow scattering to the microwave brightness temperatures. This retrieval method successfully diagnosed the LWP and WVP along the flight tracks during the CAESAR campaign in near-real-time, aiding in-flight sampling decisions.

The high spatial resolution of this new airborne LWP retrieval ( $\sim 500$  m), designed specifically for mixed-phase cold-air outbreaks, also provides a new capability to connect the CAO liquid-ice partitioning to cloud scale processes. An example, shown in Fig. 9, can be further extended with the Two-Dimensional-Stereo (2D-S), High Volume Precipitation Spectrometer-3 (HVPS3) and Particle Habit Imaging and Polar Scattering (PHIPS) cloud probes to better constrain the snow parameters within the retrieval. The combination with other CAESAR measurements will provide the full characterization needed to determine the processes supporting the closed-to-open cell transition.

The retrieval agrees well with the cloud probes across multiple research flights (Fig. 8), and diagnoses LWP maximum coincident with updrafts, similarly documented by Mages et al. (2023). The approach can be adapted to a wide variety of applications in regions where the WVP is below  $\sim 10$ -15  $\text{kg m}^{-2}$  with minimal rain water content. An important reminder is that the training data must accurately represent the same cloud regime that the retrieval is intended for.

While this demonstration highlights the benefits of multi-instrument retrievals, there are still some areas for improvement. For example, in thin clouds, in some instances the retrieval is too sensitive to changes in WCR reflectivity, causing it to diagnose small amounts of LWP (though still within the margin of error) in clouds that are likely all ice based on the Wyoming Cloud Lidar (WCL) data (University of Wyoming - Flight Center 2007), and a lack of variability in the GVR  $T_b$  time series. One possible

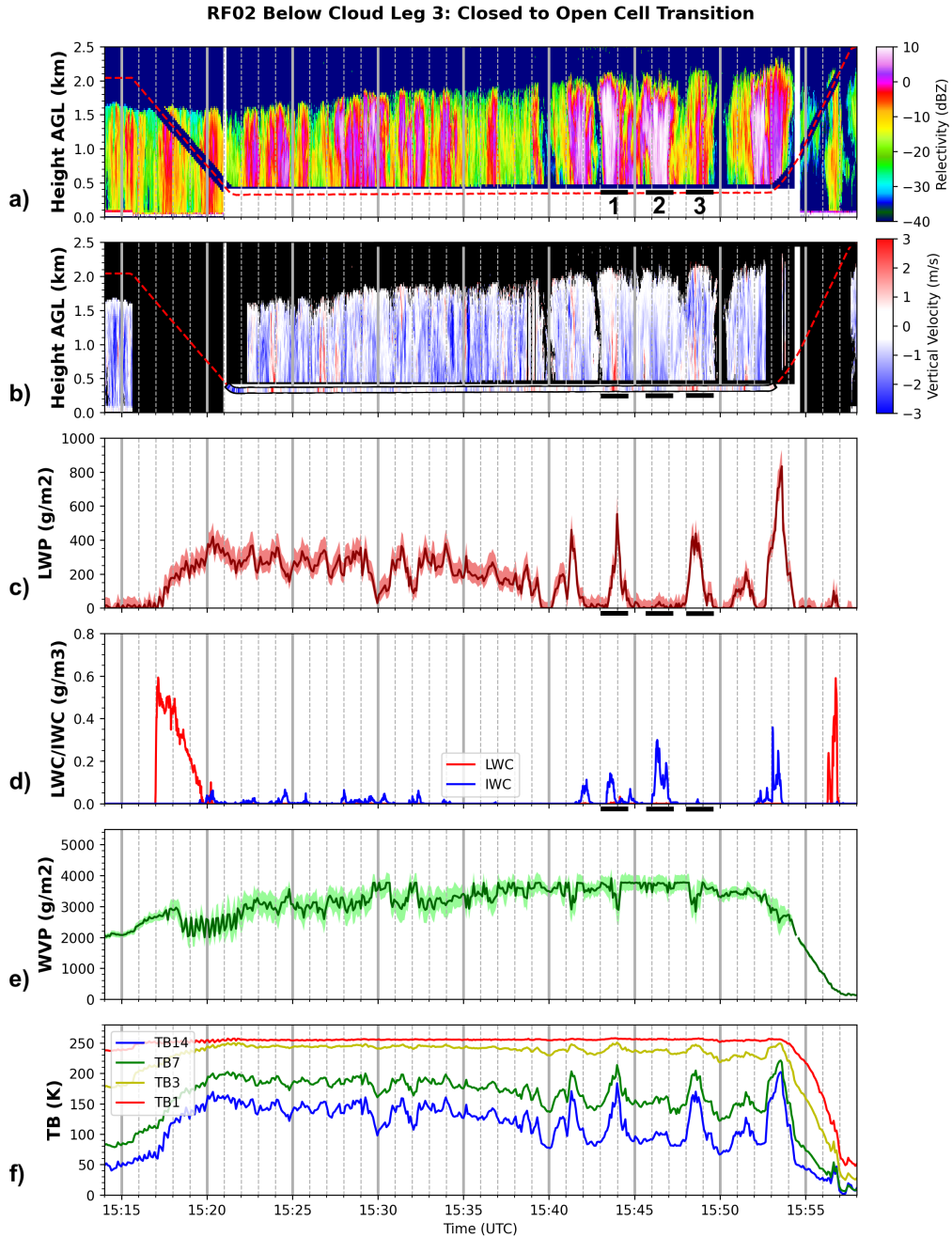


Fig. 9. Retrievals and *in-situ* data centered on a below cloud leg from February 29 2024 (RF02) across a closed to open celled transition. a) WCR reflectivity and b) Doppler velocity with *in-situ* vertical velocity included. Plane's altitude with time indicated with a dotted red line. c) LWP retrieval, d) *in-situ* CDP-derived LWC (red) and Nevzorov probe IWC (blue), e) WVP retrieval, and f) GVR  $T_b$  (bias corrected). Shaded areas in c) and e) indicate retrieval uncertainties. Three convective cells are numbered.

cause is that the riming factor in the operational retrieval does not match the observed microphysics. After an analysis of the microphysical probes and particle imagery from CAESAR, adjustments may be made to the riming factor used. In addition, further work may explore integrating

other upward-looking instruments into the retrieval, such as the WCL to better constrain the retrieval.

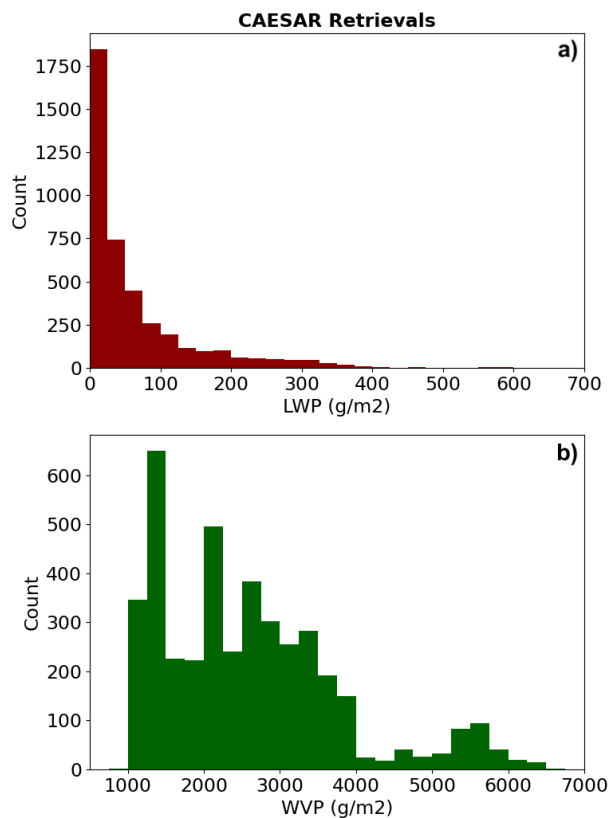


FIG. 10. Histogram of retrieved a) LWP and b) WVP during CAESAR when the C-130 was below 500 m altitude and GWR oscillations were not present (including clear sky times). A polar-low focused flight, (RF09) is not included. Based on dropsondes, an estimated 150-2000 g m<sup>-2</sup> of WVP is also present below the aircraft at these times.

*Acknowledgments.* SE and PZ gratefully acknowledge financial support through NSF AGS award number 2150848. We thank NCAR RAF and NSF for their dedication and commitment to the CAESAR project. All PAMTRA simulations were run on NSF NCAR High-Performance Computers, named Derecho and Cheyenne (Computational and Information Systems Laboratory (2024) and Computational and Information Systems Laboratory (2023)). We thank Davide Ori, Jan Chylik, and Mario Mech for their advice on the PAMTRA code.

*Data availability statement.* Datasets for all the NSF-supported CAESAR campaign are publicly available through the National Center of Atmospheric Research Earth Observing Laboratory. The retrieval results and GVR data are available at (<https://doi.org/10.26023/36JM-V39N-R408>). Documentation and retrieval code is available at (<https://github.com/ephraims28/ML-retrieval>). Data were obtained for the Southern Great Plains and North Slope of Alaska sites from the Atmospheric Radiation Measurement (ARM) user facility, managed by the U.S. Biological and Environmental Research Program for the Department of Energy Office of Science (<https://www.arm.gov/>). The PAMTRA code is publicly available through a GitHub repository distributed under a GPLv3.0 license at (<https://github.com/igmk/pamtra>). Files related to the WRF model setup, raw and post-processed WRF outputs, satellite retrievals, and analysis scripts are available in a Harvard Dataverse repository (<https://doi.org/10.7910/DVN/U3VI1X>; Juliano & Lackner, 2024).

## APPENDIX A

### Qualitative Demonstration

The premise of incorporating radar reflectivities in this study, while the retrieval of LWP in previous studies typically only use microwave methods, is that liquid cloud droplets are not the only hydrometeor contributing to measured  $T_b$ . Cloud liquid contributes to brightness through primary emission, but snow also has a secondary contribution to brightness by scattering upward emissions from the ocean back downward to the radiometer. This relationship is evident within the PAMTRA simulated  $T_b$ s and reflectivities in a 15x15 km box of the LES model run in a region of open cell convection that contained the highest LWPs (small red box in Figure 1). The hydrometeor amounts of each species are shown in the first column in Figure A1 (LWP, SWP, ice water path (IWP), graupel water path (GWP)). Water vapor path (WVP) is also evaluated. The rain water path is not included as it is negligible within the simulations.

To simulate the GVR, the  $T_b$  contributions from each individual hydrometeor species are simulated using PAMTRA at  $(183.31 \pm 14 \text{ GHz})$  in the second column of Figure A1. The  $\pm 14 \text{ GHz}$  channel was chosen since water vapor has the smallest impact on that channel, and LWP the largest of the four channels, allowing for a more vivid comparison. The primary contribution to the total  $T_b$  is from cloud liquid, with the second largest contribution coming from snow. Other hydrometeor types have negligible effects.

The WCR vertically integrated 95 GHz reflectivities of each individual hydrometeor species is also simulated by PAMTRA. The primary contribution to reflectivity is from snow, with a secondary contribution from cloud liquid. The third column in Figure A1 shows the individual hydrometeor contribution to the integrated reflectivities.

We also attempted to retrieve the total amount of frozen hydrometeors (frozen water path, FWP = snow + graupel + cloud ice) using a similar rationale to our LWP retrieval. FWP is very similar to SWP since cloud ice is present in low quantities, and graupel is present in very scattered locations. FWP is a more useful quantity than snow alone because the threshold separating snow from cloud ice in the model output is arbitrarily established. A retrieval of LWP and FWP should be achievable because we will have two unknown variables (LWP and FWP) and two known independent variables coming from measurements of the GVR and WCR. Both LWP and FWP have distinct patterns in how they impact GVR and WCR measurements. Cloud liquid dominates the GVR  $T_b$  and has a secondary contribution to WCR reflectivity. Frozen hydrometeors dominate WCR reflectivity and have a secondary contribution to GVR  $T_b$ . Unfortunately, a retrieval of FWP only worked in model testing and was not reliable in the field. This is likely due to the high sensitivity of the FWP retrieval to PAMTRA modeled reflectivities. Even small differences between the training and observed reflectivities (caused by differences in the calibration of the WCR with respect to PAMTRA simulations and our representation of the frozen microphysics in PAMTRA) were too large for a viable FWP retrieval.

### References

- Abel, S. J., and Coauthors, 2017: The role of precipitation in controlling the transition from stratocumulus to cumulus clouds in a northern hemisphere cold-air outbreak. *Journal of Atmospheric Science*, **74** (7), 2293 – 2314, <https://doi.org/10.1175/JAS-D-16-0362.1>.
- Alexandar, S. P., G. M. McFarquhar, R. Marchand, A. Protat, E. Vignon, G. G. Mace, and A. R. Klekociuk, 2021: Mixed-phase clouds and precipitation in Southern Ocean cyclones and cloud systems observed poleward of 64°S by ship-based cloud radar and lidar. *Journal of Geophysical Research: Atmospheres*, **126**.
- Bodas-Salcedo, A., T. Andrews, A. V. Karmalkar, and M. A. Ringer, 2016a: Cloud liquid water path and radiative feedbacks over the

### Hydrometeor Contributions to Brightness Temperature and Reflectivity

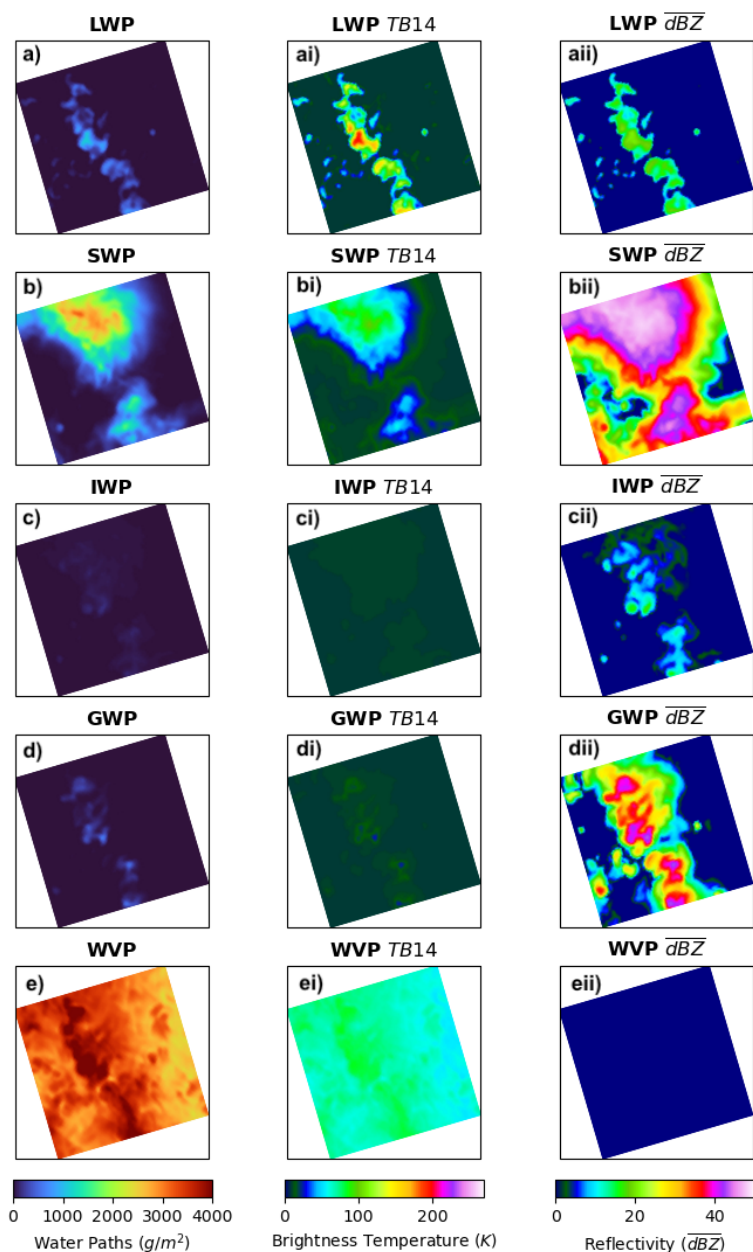


FIG. A1. The first column shows the spatial distribution of a) LWP, b) SWP, c) ice water path (IWP), d) graupel water path (GWP), and e) WVP within the red box in Fig. 1. This is a region of CAO open celled convection in an LES model simulation of 13 March 2020. The second column shows contribution of ai) LWP, bi) SWP, ci) IWP, di) GWP, and ei) WVP to the  $\pm 14$  GHz  $T_b$ . The third column shows contribution of aii) LWP, bii) SWP, cii) IWP, dii) GWP, and eii) WVP to the integrated 95 GHz reflectivities ( $\overline{dBZ}$ ).

Southern Ocean. *Geophysical Research Letters*, **43**, 10,938–10,946, <https://doi.org/10.1002/2016GL070770>.

Ocean. *Journal of Climate*, **29** (11), 4213 – 4228, <https://doi.org/10.1175/JCLI-D-15-0564.1>.

Bodas-Salcedo, A., P. G. Hill, K. Furtado, K. D. Williams, P. R. Field, J. C. Manners, P. Hyder, and S. Kato, 2016b: Large contribution of supercooled liquid clouds to the solar radiation budget of the Southern

Brandes, E. A., K. Ikeda, G. Zhang, M. Schönhuber, and R. M. Rasmussen, 2007: A statistical and physical description of hydrometeor distributions in Colorado snowstorms using a video disdrometer.

- Journal of Applied Meteorology and Climatology*, **46** (5), 634–650, <https://doi.org/10.1175/JAM2489.1>.
- Bremen, L. V., E. Ruprecht, and A. Macke, 2002: Errors in liquid water path retrieval arising from cloud inhomogeneities: The beam-filling effect. *Meteorologische Zeitschrift*, **11**, 13–19, <https://doi.org/10.1127/0941-2948/2002/0011-0013>.
- Brown, P. R. A., and P. N. Francis, 1995: Improved measurements of the ice water content in cirrus using a total-water probe. *Journal of Atmospheric and Oceanic Technology*, **12** (2), 410–414, [https://doi.org/10.1175/1520-0426\(1995\)012<0410:IMOTIW>2.0.CO;2](https://doi.org/10.1175/1520-0426(1995)012<0410:IMOTIW>2.0.CO;2).
- Cadeddu, M., and M. Tuftedal, 2021: G-band (183 GHz) vapor radiometer (GVR). Accessed 23 January 2024, <https://doi.org/10.5439/1986620>.
- Cadeddu, M. P., 2011: GVR radiometer handbook. Tech. rep., ARM.
- Cadeddu, M. P., J. C. Liljegren, and A. L. Pazmany, 2007: Measurements and retrievals from a new 183-GHz water vapor radiometer in the Arctic. *IEEE Trans. Geosci. Remote Sens.*, **45**, 2207–2215.
- Cadeddu, M. P., R. Marchand, E. Orlandi, D. D. Turner, and M. Mech, 2017: Microwave passive ground-based retrievals of cloud and rain liquid water path in drizzling clouds: Challenges and possibilities. *IEEE Transactions on Geoscience and Remote Sensing*, **55**, 6468–6481.
- Cadeddu, M. P., D. D. Turner, and J. C. Liljegren, 2009: A neural network for real-time retrievals of PWV and LWP from Arctic millimeter-wave ground-based observations. *IEEE Transactions on Geoscience and Remote Sensing*, **47**, 1887–1900, <https://doi.org/10.1109/TGRS.2009.2013205>.
- Clough, S., M. Shephard, E. Mlawer, J. Delamere, M. Iacono, K. Cady-Pereira, S. Boukabara, and P. Brown, 2005: Atmospheric radiative transfer modeling: a summary of the AER codes. *Journal of Quantitative Spectroscopy and Radiative Transfer*, **91** (2), 233–244, <https://doi.org/https://doi.org/10.1016/j.jqsrt.2004.05.058>.
- Computational and Information Systems Laboratory, 2023: Cheyenne: HPE/SGI ICE XA System (University Community Computing). Boulder, CO: NSF National Center for Atmospheric Research. <https://doi.org/doi:10.5065/D6RX99HX>.
- Computational and Information Systems Laboratory, 2024: Derecho: HPE Cray EX System (University Community Computing). Boulder, CO: NSF National Center for Atmospheric Research. <https://doi.org/10.5065/qx9a-pg09>.
- Deardorff, J. W., 1980: Stratocumulus-capped mixed layers derived from a three-dimensional model. *Boundary-Layer Meteorology*, **18**, 495–527.
- Elsaesser, G. S., C. W. O'Dell, M. D. Lebsack, R. Bennartz, T. J. Greenwald, and F. J. Wentz, 2017: The multisensor advanced climatology of liquid water path (MAC-LWP). *Journal of Climate*, **30** (24), 10 193–10 210, <https://doi.org/10.1175/JCLI-D-16-0902.1>.
- Feng, Y.-C., and Coauthors, 2021: Ka ARM zenith radar (kazrcfrge). Accessed August 30 2023, <https://doi.org/10.5439/1498936>.
- Flynn, D., and V. Morris, 2023: Total sky imager (tsiskycover). Accessed 10 January 2024, <https://doi.org/10.5439/1992207>.
- Gaussiat, N., R. J. Hogan, and A. J. Illingworth, 2007: Accurate liquid water path retrieval from low-cost microwave radiometers using additional information from a lidar, ceilometer and operational forecast models. *Journal of Atmospheric and Oceanic Technology*, **24** (9), 1562–1575, <https://doi.org/10.1175/JTECH2053.1>.
- Geerts, B., and Coauthors, 2022: The COMBLE campaign: A study of marine boundary layer clouds in Arctic cold-air outbreaks. *Bulletin of the American Meteorological Society*, **103** (5), E1371–E1389, <https://doi.org/10.1175/BAMS-D-21-0044.1>.
- Hogan, R. J., R. Honeyager, J. Tyynelä, and S. Kneifel, 2017: Calculating the millimetre-wave scattering phase function of snowflakes using the self-similar Rayleigh–Gans approximation. *Quarterly Journal of the Royal Meteorological Society*, **143** (703), 834–844, [https://doi.org/10.1002/qj.2968](https://doi.org/https://doi.org/10.1002/qj.2968).
- Hong, S.-Y., Y. Noh, and J. Dudhia, 2006: A new vertical diffusion package with an explicit treatment of entrainment processes. *Monthly Weather Review*, **134**, 2318–2341.
- Hu, Y., and Coauthors, 2023: Vertical structure and ice production processes of shallow convective postfrontal clouds over the Southern Ocean in MARCUS. Part I: Observational study. *Journal of the Atmospheric Sciences*, **80** (5), 1285–1306, <https://doi.org/10.1175/JAS-D-21-0243.1>.
- Huang, X., P. R. Field, B. J. Murray, D. P. Grosvenor, F. van den Heuvel, and K. S. Carslaw, 2025: Different responses of cold-air outbreak clouds to aerosol and ice production depending on cloud temperature. <https://doi.org/10.5194/egusphere-2024-4070>.
- Juliano, T. W., C. P. Lackner, B. Geerts, B. Kosovic, L. Xue, P. Wu, and J. Olson, 2024: Simulating mixed-phase open cellular clouds observed during COMBLE: Evaluation of parameterized turbulence closure. *Journal of Geophysical Research: Atmospheres*, **129**, <https://doi.org/10.1029/2024JD040889>.
- Juliano, T. W., and Coauthors, 2022: Smoke from 2020 United States wildfires responsible for substantial solar energy forecast errors. *Environmental Research Letters*, **17**.
- Keeler, E., K. Burk, and J. Kyrouac, 2023: Balloon-borne sounding system (sondewnpn). Accessed 23 January 2024, <https://doi.org/10.5439/1595321>.
- Khanal, S., Z. Wang, and J. R. French, 2020: Improving middle and high latitude cloud liquid water path measurements from MODIS. *Atmospheric Research*, **243**, 105 033, <https://doi.org/https://doi.org/10.1016/j.atmosres.2020.105033>.
- Kingma, D. P., and J. Ba, 2017: Adam: A method for stochastic optimization. URL <https://arxiv.org/abs/1412.6980>.
- Kirbus, B., J. Chylik, A. Ehrlich, S. Becker, M. Schäfer, R. Neggers, and M. Wendisch, 2023: Analysis of an Arctic cold air outbreak during autumn and related air mass transformations forced by surface changes and advection in higher altitudes. *Elem. Sci. Anth.*, **11**.
- Kolstad, E. W., and T. J. Bracegirdle, 2008: Marine cold-air outbreaks in the future: an assessment of IPCC AR4 model results for the Northern Hemisphere. *Climate Dynamics*, **30**, 871–885, <https://doi.org/10.1007/s00382-007-0331-0>.
- Korolev, A., and Coauthors, 2017: Mixed-Phase Clouds: Progress and Challenges. *Meteorological Monographs*, **58**, 5.1–5.50, <https://doi.org/10.1175/AMSMONOGRAPHS-D-17-0001.1>.
- Korolev, A. V., J. W. Strapp, G. A. Isaac, and A. N. Nevzorov, 1998: The Nevzorov Airborne Hot-Wire LWC–TWC probe: Principle of operation and performance characteristics. *Journal of Atmospheric*

- and *Oceanic Technology*, **15**, 1495–1510, [https://doi.org/10.1175/1520-0426\(1998\)015\(1495:TNAHWL\)2.0.CO;2](https://doi.org/10.1175/1520-0426(1998)015(1495:TNAHWL)2.0.CO;2).
- Lackner, C. P., B. Geerts, T. W. Juliano, B. Kosovic, and L. Xue, 2024: Characterizing mesoscale cellular convection in marine cold air outbreaks with a machine learning approach. *Journal of Geophysical Research: Atmospheres*, **129**, <https://doi.org/10.1029/2024JD041651>.
- Lance, S., 2012: Coincidence errors in a cloud droplet probe (CDP) and a cloud and aerosol spectrometer (CAS), and the improved performance of a modified CDP. *Journal of Atmospheric and Oceanic Technology*, **29** (10), 1532 – 1541, <https://doi.org/10.1175/JTECH-D-11-00208.1>.
- Lance, S., C. A. Brock, D. Rogers, and J. A. Gordon, 2010: Water droplet calibration of the cloud droplet probe (CDP) and in-flight performance in liquid, ice and mixed-phase clouds during ARCPAC. *Atmospheric Measurement Techniques*, **3** (6), 1683–1706, <https://doi.org/10.5194/amt-3-1683-2010>.
- Liljegren, J., 2004: Improved retrievals of temperature and water vapor profiles with a twelve-channel radiometer. *Bulletin of the American Meteorological Society*.
- Liljegren, J. C., E. E. Clothiaux, G. G. Mace, S. Kato, and X. Q. Dong, 2001: A new retrieval for cloud liquid water path using a ground-based microwave radiometer. *J. Geophys. Res.*, **102**, 8703 – 8718.
- Maahn, M., D. D. Turner, U. Löhnert, D. J. Posselt, K. Ebell, G. G. Mace, and J. M. Comstock, 2020: Optimal estimation retrievals and their uncertainties: What every atmospheric scientist should know. *Bulletin of the American Meteorological Society*, **101** (9), E1512 – E1523, <https://doi.org/10.1175/BAMS-D-19-0027.1>.
- Mages, Z., P. Kollias, Z. Zhu, and E. P. Luke, 2023: Surface-based observations of cold-air outbreak clouds during the COMBLE field campaign. *Atmospheric Chemistry and Physics*, **23**, 3561–3574, <https://doi.org/10.5194/acp-23-3561-2023>.
- Mason, S. L., C. J. Chiu, R. J. Hogan, D. Moisseev, and S. Kneifel, 2018: Retrievals of riming and snow density from vertically pointing Doppler radars. *Journal of Geophysical Research: Atmospheres*, **123** (24), 13,807–13,834, <https://doi.org/https://doi.org/10.1029/2018JD028603>.
- Mason, S. L., R. J. Hogan, C. D. Westbrook, S. Kneifel, D. Moisseev, and L. von Terzi, 2019: The importance of particle size distribution and internal structure for triple-frequency radar retrievals of the morphology of snow. *Atmospheric Measurement Techniques*, **12** (9), 4993–5018, <https://doi.org/10.5194/amt-12-4993-2019>.
- McCluskey, C. S., and Coauthors, 2023: Simulating Southern Ocean aerosol and ice nucleating particles in the Community Earth System Model Version 2. *Geophysical Research Letters*, **128** (8), e2022JD036955, <https://doi.org/https://doi.org/10.1029/2022JD036955>.
- McGrath, A., and T. Hewison, 2001: Measuring the accuracy of MARSS—an airborne microwave radiometer. *Journal of Atmospheric and Oceanic Technology*, **18** (12), 2003 – 2012, [https://doi.org/10.1175/1520-0426\(2001\)018\(2003:MTAOMA\)2.0.CO;2](https://doi.org/10.1175/1520-0426(2001)018(2003:MTAOMA)2.0.CO;2).
- Mech, M., M. Maahn, S. Kneifel, D. Ori, E. Orlandi, P. Kollias, V. Schemann, and S. Crewell, 2020: PAMTRA 1.0: the Passive and Active Microwave radiative TRAnsfer tool for simulating radiometer and radar measurements of the cloudy atmosphere. *Geoscientific Model Development*, **13** (9), 4229–4251, <https://doi.org/10.5194/gmd-13-4229-2020>.
- Miles, N. L., J. Verlinde, and E. E. Clothiaux, 2000: Cloud droplet size distributions in low-level stratiform clouds. *Journal of the Atmospheric Sciences*, **57** (2), 295 – 311, [https://doi.org/10.1175/1520-0469\(2000\)057<0295:CDSIDL>2.0.CO;2](https://doi.org/10.1175/1520-0469(2000)057<0295:CDSIDL>2.0.CO;2).
- Morrison, H., G. de Boer, G. Feingold, J. Harrington, M. D. Shupe, and K. Sulia, 2012: Resilience of persistent Arctic mixed-phase clouds. *Nature Geoscience*, **1**, 11–17, <https://doi.org/10.1038/ngeo1332>.
- Olson, J. B., J. S. Kenyon, W. Angevine, J. M. Brown, M. Pagowski, and K. Sušelj, 2019: A description of the MYNN-EDMF scheme and the coupling to other components in WRF-ARW. <https://doi.org/10.25923/n9wm-be49>.
- Pazmany, A. L., 2007: A compact 183-GHz radiometer for water vapor and liquid water sensing. *IEEE Transactions on Geoscience and Remote Sensing*, **45** (7), 2202–2206, <https://doi.org/10.1109/TGRS.2006.888104>.
- Pedregosa, F., and Coauthors, 2011: Scikit-learn: Machine learning in python. *Journal of Machine Learning Research*, **12** (Oct), 2825–2830.
- Raif, E. N., and Coauthors, 2024: High ice-nucleating particle concentrations associated with Arctic haze in springtime cold-air outbreaks. *Atmos. Chem. Phys.*, **24**, 14 045–14 072.
- Reynolds, R. W., T. M. Smith, C. Liu, D. B. Chelton, K. S. Casey, and M. G. Schlax, 2007: Daily high-resolution-blended analyses for sea surface temperature. *Journal of Climate*, **20** (22), 5473 – 5496, <https://doi.org/10.1175/2007JCLI1824.1>.
- Rosenkranz, P. W., 1998: Water vapor microwave continuum absorption: A comparison of measurements and models. *Radio Science*, **33** (4), 919–928, <https://doi.org/https://doi.org/10.1029/98RS01182>.
- Seethala, C., and Coauthors, 2024: Microphysical evolution in mixed-phase mid-latitude marine cold-air outbreaks. *Journal of Atmospheric Science*, **81**, <https://doi.org/10.1175/JAS-D-23-0203>.
- Sieron, S., F. Zhang, E. E. Clothiaux, and L. Yinghui, 2017: Coupling WRF microphysics parameterizations to community radiative transfer model simulations of microwave frequencies, towards data assimilation for tcs, pSU-UMD DA Workshop.
- Skamarock, W. C., and J. B. Klemp, 2008: A time-split nonhydrostatic atmospheric model for weather research and forecasting applications. *Journal of Computational Physics*, **227**, 3465–3485.
- Skamarock, W. C., and Coauthors, 2019: A description of the Advanced Research WRF version 4. *NCAR Tech. Note NCAR/TN-556+STR*.
- Thompson, G., and T. Eidhammer, 2014: A study of aerosol impacts on clouds and precipitation development in a large winter cyclone. *Journal of Atmospheric Science*, **71**, 3636–901.
- Turner, D. D., S. A. Clough, J. C. Liljegren, E. E. Clothiaux, K. E. Cady-Pereira, and K. L. Gaustad, 2007: Retrieving liquid water path and precipitable water vapor from the Atmospheric Radiation Measurement (ARM) microwave radiometers. *IEEE Transactions on Geoscience and Remote Sensing*, **45** (11), 3680–3690, <https://doi.org/10.1109/TGRS.2007.903703>.
- Ulaby, F., R. Moore, and A. Fung, 1986: *Microwave Remote Sens.: Active and Passive. Vol. III. From theory to applications*. Artech House Publishers, <https://doi.org/10.1017/S0016756800015831>.
- University of Wyoming - Flight Center, 1995: University of Wyoming Cloud Radar (WCR). <https://doi.org/10.15786/M2237S>.

- University of Wyoming - Flight Center, 2007: University of Wyoming Cloud Lidar (WCL). <https://doi.org/10.15786/M25W9D>.
- Walbröl, A., H. J. Griesche, M. Mech, S. Crewell, and K. Ebell, 2024: Combining low and high frequency microwave radiometer measurements from the MOSAiC expedition for enhanced water vapour products. *Atmospheric Measurement Techniques*, **17**, 6223–6245, <https://doi.org/10.5194/amt-17-6223-2024>.
- Walbröl, A., and Coauthors, 2022: Atmospheric temperature, water vapour and liquid water path from two microwave radiometers during MOSAiC. *Scientific Data*, **9**, <https://doi.org/10.1038/s41597-022-01504-1>.
- Wang, Y., B. Geerts, and Y. Chen, 2016: Vertical structure of boundary layer convection during cold-air outbreaks at Barrow, Alaska. *Journal of Geophysical Research: Atmospheres*, **121** (1), 399–412, <https://doi.org/10.1002/2015JD023506>.
- Wang, Z., and Coauthors, 2012: Single aircraft integration of remote sensing and in situ sampling for the study of cloud microphysics and dynamics. *Bulletin of the American Meteorological Society*, **93** (5), 653 – 668, <https://doi.org/10.1175/BAMS-D-11-00044.1>.
- Wendisch, M., and Coauthors, 2024: Overview: quasi-lagrangian observations of Arctic air mass transformations – introduction and initial results of the HALO–(AC)3 aircraft campaign. *Atmospheric Chemistry and Physics*, **24**, 8865–8892.
- Zuidema, P., and R. Joyce, 2008: Water vapor, cloud liquid water paths, and rain rates over the northern high latitude open seas. *Journal of Geophysical Research: Atmospheres*, **113**, <https://doi.org/10.1029/2007JD009040>.
- Zuidema, P., D. Leon, A. Pazmany, and M. Cadeddu, 2012: Aircraft millimeter-wave passive sensing of cloud liquid water and water vapor during VOCALS-REx. *Atmospheric Chemistry and Physics*, **12**, 355–369, <https://doi.org/10.5194/acp-12-355-2012>.
- Zuidema, P., E. R. Westwater, C. Fairall, and D. Hazen, 2005a: Ship-based liquid water path estimates in marine stratocumulus. *J. Geophys. Res.*, **110**, <https://doi.org/10.1029/2005JD005833>.
- Zuidema, P., and Coauthors, 2005b: An Arctic springtime mixed-phase cloudy boundary layer observed during SHEBA. *Journal of Atmospheric Science*, **62**, 160–176.